First-principles localized cluster expansion study of the kinetics of hydrogen diffusion in homogeneous and heterogeneous Fe-Cr alloys

Adib J. Samin, David A. Andersson, Edward F. Holby, and Blas P. Uberuaga

Phys. Rev. B **99**, 014110 — Published 23 January 2019

DOI: 10.1103/PhysRevB.99.014110

A first-principles localized cluster expansion study of the kinetics of hydrogen diffusion in homogeneous and heterogeneous Fe-Cr alloys

Adib J. Samin[a], David A. Andersson[a], Edward F. Holby[b], and Blas P. Uberuaga[a]

[(a)] Materials Science and Technology Division, Los Alamos National Laboratory,

Los Alamos, New Mexico 87545, USA

[(b)] Sigma Division, Los Alamos National Laboratory,

Los Alamos, New Mexico 87545, USA

Abstract:

Metal alloys have a wide range of technological applications, from structural materials to catalysts. In many situations the transport of hydrogen, whether intentionally for hydrogen storage and fuel cell applications or unintentionally in the case of tritium uptake in nuclear materials, is an important concern. Fe-Cr binary alloys, in particular, may be viewed as a simple model system to represent ferritic steels used in nuclear energy systems and, more generally, as a model binary alloy for examining the role of alloying elements on transport. In this work, we used density functional theory, cluster expansion, and kinetic Monte Carlo to study hydrogen kinetics in Fe-Cr alloys. In random homogenenous alloys, we observed that hydrogen diffusivity first decreased with increasing Cr content and then increased to its levels in pure Cr. Furthermore, the effects of heterogeneity, as might be induced by irradiation, were explored and it was concluded that local structural heterogeneities for the same overall Cr concentration may significantly affect the hydrogen diffusivity. The effect was attributed to the relative binding energy of hydrogen in different metals and this understanding was then utilized to predict hydrogen transport behavior in different element-segregated grain/grain boundary combinations and thus identify solute/solvent alloys where hydrogen transport might be either hindered or

enhanced. Finally, we comment on the potential impact of radiation-induced segregation on hydrogen behavior in nuclear energy systems.

Introduction:

Metallic alloys have wide ranging applications across the structural, medical, automobile and aerospace industries and play a significant role in all sectors of the economy. Hydrogen is known to negatively affect the mechanical properties of structural metals, a process known as hydrogen embrittlement [1-3]. This process, involving the accumulation of hydrogen at local microstructural defects, may lead to the degradation of steels and is an important limiting factor in the operational lifetime of structural materials and medical implants [4-7]. In some cases, however, the uptake and packing of hydrogen may be desired such as in hydrogen storage materials for energy purposes [8, 9]. Furthermore, the study of deuterium and tritium trapping in metallic alloys is a significant issue for fusion reactors [10, 11]. The use of hydrogen has also emerged in thermohydrogen processing, a process by which hydrogen is utilized as a temporary alloying element to enhance the processability of metal alloys and manipulating their microstructure to improve final mechanical properties [12]. Therefore, establishing the fundamental science which governs the binding and transport of hydrogen in metals is of great interest for a variety of applications and may enable the future design of embrittlement-resistant alloys for structural materials or efficient hydrogen storage metals.

Ferritic stainless steels possess a bcc structure similar to alpha iron and a high chromium content ranging from 2 to 20 at%. These alloys are low cost, radiation resistant, and exhibit favorable properties such as a high melting point and good ductility. Furthermore, they are corrosion-resistant due to the high chromium content. These iron-chromium steel alloys may be utilized as structural materials for light water reactors [13, 14], nuclear fusion reactors [15, 16], and for solid oxide fuel cell applications [17, 18]. They are also promising structural materials for

Generation IV reactors [19]. The bcc Fe-Cr binary alloy represents a model system for ferritic steels and for binary alloys in general and has therefore been the subject of various recent studies [20-25].

Given the relevance of hydrogen storage and transport for a variety of applications, it is not surprising that hydrogen transport in Fe and steel alloys has been recently examined by several investigators [26-31]. However studies on Fe-based alloys have been limited thus far. Theoretical studies have primarily focused on H behavior in pure Fe. Jiang and Carter [27] studied interstitial hydrogen absorption and diffusion on bcc iron surfaces and through bulk Fe from first principles. The authors reported that hydrogen preferred to stay on surfaces instead of in the bulk. They also calculated endothermic hydrogen dissolution in Fe and that the tetrahedral (T) sites are preferable for binding hydrogen. Moreover, the dissolution energy of H in the T-site was found to change only slightly with the H concentration which implied that H-H interactions played a negligible role. Finally, it was determined that hydrogen mobility is high in bulk Fe due to low migration energy barriers. In the study, it was asserted that H diffused via hopping between neighboring T sites in a curved trajectory and that the straight path going through the octahedral (O) sites was excluded "due to its higher barrier and the rank of the saddle point"..

Sanchez et al. [32] also utilized density functional theory (DFT) calculations to investigate equilibrium geometries and diffusion barriers for hydrogen as an interstitial in bcc iron. The authors accounted for the effects of stress in their study and concluded that for low concentrations hydrogen is absorbed near the T-site to minimize elastic energy on nearby cells. Furthermore, the results of the study indicated that external stresses of several GPa modify the barriers by about 10% and the diffusion rates by about 30%. Du et al.[33] employed a kinetic Monte Carlo (kMC) model whose parameters were populated from first principles calculations to

explore hydrogen diffusion within idealized grains of bcc iron. When H-H interactions were accounted for within the idealized grains the qualitative behavior of diffusivity as a function of H concentration did not change however the dip in diffusivity occurred at much lower H concentrations. Hayward and Fu [26] utilized ab initio and classical molecular dynamics to study the interactions of hydrogen and vacancies in bcc iron. The authors emphasized the importance of accounting for zero-point energy corrections when considering light elements such as hydrogen. In this work, both T-O-T and T-T pathways were accounted for and the authors reported barriers of 0.035 eV and 0.044 eV, respectively, when using density functional theory (DFT) and barriers of 0.04 and 0.049 eV when using EAM potentials. It was concluded that hydrogen has a low diffusion barrier but may be strongly trapped in vacancies and that high local concentrations of hydrogen increase the likelihood of vacancy formation and stabilize vacancy clusters. It was further illustrated how small hydrogen-vacancy clusters diffuse by dissociation and that trivacancies are capable of dragging hydrogen.

There has been less fundamental work on H in Fe alloys. Penalva et al. [34] experimentally analyzed the influence of Cr content on the permeation of hydrogen in Fe base alloys, measuring the hydrogen transport permeability in pure Fe metal, Fe5%Cr alloy and Fe10%Cr alloy in the temperature range of 423 - 823 K. They found that the permeability for the three materials under scrutiny followed an Arrhenius law with the activation energies increasing with Cr content in the alloy, which led to smaller values of the permeability for the cases being examined. Bruzzoni et al. [25] recently conducted a DFT study of hydrogen solubility and diffusivity in the $Fe_{15}Cr$ alloy by utilizing a 16 atom supercell. The study suggested that the substitutional Cr atom repelled H and the diffusion coefficient was found to be reduced by 13% when compared with pure Fe.

Other binary alloys are important for a number of technological applications. Thus, hydrogen transport and behavior in other binary alloys has been studied by a number of investigators. Ke and Kramer [35] studied hydrogen diffusion in palladium silver using DFT and observed that hydrogen should avoid the Ag-rich areas. Kamakoti and Sholl [36] examined hydrogen diffusion in CuPd alloys with compositions greater than 47 at% Pd. The authors used a combination of DFT, a lattice gas model, and kMC techniques in their work, computed H diffusivities as a function of alloy composition and temperatures ranging from 400 K to 1200 K, and determined the effects of short-range order to be small under the conditions of experimental interest. Their work was deemed to agree well with the available experimental data. In 2008, Semidey-Flecha and Sholl [37] used DFT and cluster expansion methods to describe the behavior of interstitial H in alloys of composition $Pd_{96}M_4$ (M=Ag, Cu, and Rh) and to predict H_2 permeance through these alloy membranes. Adding a small amount of Ag to pure Pd was determined to enhance the H diffusion while the opposite effect was observed when either Cu or Rh were used. These observations were also qualitatively consistent with experimental work. Lu et al. [38] conducted a first principles study of hydrogen behavior in vanadium-based binary alloy membranes and found the elastic effect to be a significant factor in affecting hydrogen dissolution in $V_{15}M$. The authors also concluded that additions of Al, Ti and Nb improved the hydrogen diffusion coefficient in vanadium.

Despite this body of work, there are still important questions that must be answered. In particular, previous theoretical studies that considered H transport in alloys either focused on very specific compositions and/or purely random distributions of the alloying element. Thus, how chemical heterogeneities in the material nanostructure might impact H transport is an open

question. In the context of Fe-Cr alloys proposed as clad materials in accident tolerant fuels, hydrogen transport through the alloy dictates whether tritium can leak from the fuel rod and into the coolant, which is detrimental to reactor operation [39-41]. Given that radiation naturally redistributes alloying elements such as Cr [40-42], understanding how chemical heterogeneities impact transport is important for predicting how H evolution will occur as the fuel burns. In other contexts, understanding hydrogen behavior in heterogeneous structures may be significant for composites which are used for hydrogen storage [43, 44] or hydrogen production [45] to enable an efficient use of hydrogen as a source of clean energy.

In this work, we utilized a DFT-parameterized kinetic Monte Carlo (kMC) approach to study hydrogen transport through Fe-Cr binary alloys. This was accomplished by generating a DFT database of H binding in varied alloy structures which was used to fit a localized cluster expansion description of the binding energy as a function of local structure and then calculating the barriers of hydrogen transport through different pathways. This methodology allowed us to examine the behavior of hydrogen kinetics in the entire range of Fe-Cr alloy compositions without being limited to the cases of dilute chromium as in previous works. In addition, we examined the effects of chemical heterogeneities on hydrogen trapping and transport. This is especially important in the context of radiation damage where segregation may lead to chromium-rich regions [40-42]. General trends in H transport as a function of alloy content and local chemical environments were identified and applied to some of the outstanding questions related to H diffusion through alloy systems.

Computational Methods:

A. DFT Calculations:

Spin polarized density functional theory calculations were carried out using the Vienna ab initio simulation package (VASP) [46] with the implementation of the Projector-Augmented-Wave (PAW) pseudopotentials [47, 48]. The generalized gradient approximation (GGA) exchange correlation functional was used as parameterized by Perdew, Burke and Ernzerhov [49]. The valence electron eigenfunctions were expanded in a plane-wave basis set with an energy cutoff of 500 eV. The Fermi level was smeared using a Methfessel-Paxton smearing of the first order of width 0.05 eV in all calculations [50]. The convergence criterion for the electronic self-consistent calculation was set to 10^{-6} eV. Furthermore, the structure was allowed to relax until the total calculated energy difference between successive calculations was less than 10^{-4} eV. First, DFT calculations were performed on the unit cells of bcc Fe and bcc Cr in order to determine the optimal lattice constant for the pseudopotentials used. Reciprocal length integrations were performed using a (18×18×18) Monkhorst-Pack [51] Γ-centered k-point grid. Next, 3×3×3 supercells of pure iron, pure chromium and Fe-Cr binary alloys (a total of 54 atoms) were prepared by randomly placing the atoms at the bcc lattice positions. Four compositions were explored: $Fe_{0.95}Cr_{0.05,}$ $Fe_{0.9}Cr_{0.1,}$ $Fe_{0.8}Cr_{0.2}$ and $Fe_{0.1}Cr_{0.9}$. The first three structures represent steel alloys whereas the last structure was examined in order to represent the chromium-rich α′ phase which may form as a result of species segregation during radiation-exposure [42, 52, 53]. For each of these compositions, three different representations of the alloy were produced by random assignment to allow for chemical variation and statistics. Moreover, the atoms were relaxed in the DFT calculation using a 6×6×6 Monkhorst-Pack Γ-centered k-point mesh but the volume was kept fixed as previous work [27] has predicted a very small change in volume. The lattice constant used for each calculation was linearly interpolated between the lattice constants of bcc iron and bcc chromium depending on the total composition.

Furthermore, for each of these random representations, four tetrahedral sites were randomly selected and a hydrogen binding energy calculation at that T-site with atomic relaxation was performed using the same parameters as before. Thus, this gave us 64 binding energies for H in chemically unique local environments. Finally, the cluster expansion model was parametrized using these 64 binding energies and a Monte Carlo simulation was performed to search for the lowest binding energy configurations. The output of our Monte Carlo simulation was consequently fed to the DFT calculation and added to the database. This process was repeated 6 times resulting in a DFT database containing a total of 70 H binding energies.

Zero-point corrections for the calculated binding energies were accounted for in the pure iron and pure chromium cases. For these calculations, only the hydrogen atom was displaced by 0.01 □ in six directions in computing the dynamical matrix *via* finite differences. It was enough to displace the hydrogen atom by itself due to the mass difference between H on one hand and Fe/ Cr on the other [27].In addition, a 4×4×4 k-point mesh was utilized here to reduce the computational load. Climbing Image Nudged Elastic Band (CI-NEB) calculations [54] were also performed to identify the transition state for H migration between sites. One image was utilized here and the calculations were terminated when the total force on each atom dropped below 0.01 eV/Å.

B. Localized Cluster Expansion and kinetic Monte Carlo:

The cluster expansion is a generalized Ising model containing many-body interactions. In this study, a local cluster expansion about the tetrahedral site was performed using 14 parameters. The expansion included a zero-body figure (representing the tetrahedral site), four one-body figures up to the third nearest neighbor, six two-body figures up to the second nearest neighbor,

three three-body figures up to the second nearest neighbor and one four-body figure up to the first nearest neighbor. The local cluster expansion may be described by the following equation:

$$E_b{}^{CE}(\boldsymbol{\sigma}) = J_o + \sum_{\alpha} J_\alpha \langle \prod_{i \epsilon \alpha} \sigma_i \rangle \quad (1)$$

In equation (1), the sum runs over all symmetrically inequivalent clusters. Each lattice site (i) is assigned an occupation variable $\sigma_i = +1 \; or \; -1$ depending on whether it is occupied by an Fe (-1) or a Cr (+1) atom. The angular brackets indicate an average being taken for all clusters symmetrically equivalent to cluster α. In equation 1, the *J* values represent the effective cluster interactions (ECIs). J_0 represents the zero-body structure that physically corresponds to the hydrogen occupying a T-site without interactions with any surrounding metal atoms, J_1 represents a one-body structure (physically corresponding to one metal atom in the figure), J_2 a two-body figure and so on. In the local cluster expansion, equivalent structures derived from point symmetry about the tetrahedral site were treated as degenerate. In other words, no translations were included here as the clusters were localized about the tetrahedral site and interactions between hydrogen atoms occupying different tetrahedral sites were ignored, except for a simple blocking model used in the kinetic Monte Carlo model. In the blocking model, only one hydrogen atom was allowed to occupy a single T-site at a time. This local cluster expansion was then fit to the hydrogen binding energy from the aforementioned DFT database including 70 fully relaxed structures encompassing several alloy compositions (with randomized structures) as mentioned earlier. The binding energy was computed both for T-sites and O-sites by using the fully relaxed DFT calculation for that specific alloy (of composition $Fe_{1-x}Cr_x$ with $0 \leq x \leq 1$) and half the energy of the hydrogen molecule as reference according to the equation:

$$E_b = E(Fe_{1-x}Cr_xH) - E(Fe_{1-x}Cr_x) - \frac{1}{2}E(H_2) \quad (2)$$

With this definition, a positive binding energy means that H prefers to be in the gas reference state rather than in the solid. More importantly, however, it provides a common reference for comparing H energetics in different environments within the solid. In an effort to reduce the computational effort of computing the zero-point energies (ZPEs) for each data point in our DFT database, we chose to include the zero-point energy corrections by interpolating between the ZPE values for H in bcc Fe and H in bcc Cr based on the local concentration environment in the 1st nearest neighbor shell of the alloy.

Finally, kMC simulations were performed to determine hydrogen transport properties for different alloys. In the kMC, we utilized a kinetically-resolved activation barrier model [55-57] to determine the barrier height. We further added a caveat to this barrier definition to ensure that the saddle point is higher in energy than both the initial and final states. Therefore, we defined the barrier for traversing from state *i* to state *j* as follows:

$$E_{barrier}(i \to j) = \begin{cases} \frac{E_j - E_i}{2} + E_o & if\ E_j \geq E_i\ and\ E_j - E_i \leq \frac{E_j - E_i}{2} + E_o \\ E_j - E_i + 0.01 & if\ E_j \geq E_i\ and\ E_j - E_i \geq \frac{E_j - E_i}{2} + E_o \\ \frac{E_i - E_j}{2} + E_o - E_i & if\ E_i \geq E_j\ and\ E_i - E_j \leq \frac{E_i - E_j}{2} + E_o \\ 0.01 & if\ E_i \geq E_j\ and\ E_i - E_j \geq \frac{E_i - E_j}{2} + E_o \end{cases} \quad (3)$$

In this definition, the minimum barrier for an event was defined to be 0.01 eV, to ensure that there was always some finite rate associated with the process and E_o was obtained via interpolating between the values of the ZPE-corrected energy barriers for a hop in pure Fe and pure Cr based on examining the 1st nearest neighbor shells for the initial and final states of the hop in the alloy. A rejection-free kMC method was employed to time-evolve the system and quantify H interstitial diffusion. Periodic boundary conditions (PBCs) were utilized in all directions. The hopping rate (R_q) for hop process q was given by harmonic transition state theory

[58] as $R_q = \nu e^{-\frac{E_{barrier,q}}{k_B T}}$ where ν is the attempt frequency calculated using the Vineyard approach [59], $E_{barrier,q}$ is the energy barrier for process q (derived from equation 3), k_B is the Boltzmann constant, and T is the absolute temperature. Furthermore, we attempted to go beyond the very simplest version of this model with a chemically-dependent base barrier. The interpolation for the base barrier E_o is as follows:

$$E_o = E_o(in\ bcc\ Fe) + \left(\frac{\#\ Cr\ atoms\ in\ 1st\ nn\ shell\ for\ initial\ and\ final\ state}{total\ number\ of\ atoms\ in\ 1st\ nn\ shell\ for\ initial\ and\ final\ state}\right) E_o(in\ bcc\ Cr)$$

At each kMC step, the total sum for all possible processes in the system $R_{tot} = \sum_{n=0}^{N-1} R_n$ (for N total possible processes) is computed, a random number $u_1 \in [0, R_{tot}]$ is chosen and then a process *n* is selected such that $\sum_{p=0}^{n-1} R_p < u_1 \leq \sum_{p=0}^{n} R_p$. At the end of each pass, the simulation time was evolved by $\Delta t = \frac{-\ln(u_2)}{R_{tot}}$ with a second random number $0 \leq u_2 \leq 1$. In our simulations, diffusion coefficients were calculated by running each simulation for at least 10^6 steps and discarding the first 10^4 steps (to eliminate any transient behavior). These numbers were determined by recording the mean squared displacement for each simulation and using equation (4)[60, 61]:

$$D = \lim_{t\to\infty} \frac{1}{2dtN_H} \sum_{i=1}^{N_H} \|\boldsymbol{r_i}(t) - \boldsymbol{r_i}(0)\|^2 \quad (4)$$

where t refers to time, d is the dimensionality of the simulation (d = 3 for most cases in this work, unless we quantify diffusivity in a given direction), N_H refers to the total number of hydrogen atoms in the simulation, and $\boldsymbol{r_i}(t)$ expresses the position of atom *i* at time t. Thus, D is

a measure of the H diffusivity in the simulation averaged over the trajectories of the N_H atoms used in the simulation.

Results:

A. Stability of H in Fe-Cr

We first describe our results on the properties of pure Fe and Cr as a check on the validity of our DFT calculations. Through a systematic investigation of the energy of the pure Fe lattice and a Birch-Murnaghan equation of state fit [60, 61], the optimal lattice constant *a* was calculated to be (2.83 Å) and the bulk modulus was determined to be 180 GPa. The pressure derivative of the bulk modulus was obtained as 8.6 and the local magnetic moment was 2.2 μ_B/atom, consistent with previous first principles results reporting a lattice constant of 2.834 Å, a bulk modulus of 174 GPa and the same magnetic moment [27]. For bcc Cr, it was determined that the optimal lattice constant for the pseudopotential used was 2.84 Å. The corresponding bulk modulus from the Birch-Murnaghan equation of state fit was determined to be 260 GPa and the Cr unit cell was found to be non-magnetic. These observations are again in accordance with other DFT studies [62, 63] which also used a GGA pseudopotential with the Projector Augmented Wave (PAW) method and reported a nonmagnetic structure. You et al. [63] reported a lattice constant of 2.84 Å and a bulk modulus of 258 GPa. Hafner et al.'s study [62] was more nuanced. In that calculation, the authors reported a structure with a total magnetic moment of zero, a lattice constant of 2.836 Å, and bulk modulus of 261 GPa. The authors of that study however did find that the antiferromagnetic arrangement of Cr is slightly more stable but we will later discuss how this is expected to have little effect on the H binding energy.

Next, the hydrogen binding energy was calculated for both octahedral and tetrahedral sites in both pure Fe and pure Cr. These calculations were performed according to equation 2 on

(3×3×3) supercells to minimize the interactions between the hydrogen atom and its images. This supercell was chosen consistent with previous work [27] which showed that the hydrogen binding energy negligibly changed by increasing the supercell size beyond that. The results are summarized in Table 1:

***Table 1. The binding energy of one hydrogen atom to the tetrahedral and octahedral sites of a 3×3×3 supercell of the metal as calculated from DFT. The table shows the uncorrected binding energy, the zero point energy (ZPE) attributed to the hydrogen atom in the interstitial site and the ZPE corrected values for the binding energy. The reference state of hydrogen in the H_2* molecule has a ZPE of 0.134 eV/H.**

	Fe T-site	**Fe O-site**	**Cr T-site**	**Cr O-site**
Uncorrected Binding Energy (eV)	0.24	0.39	0.63	0.80
Interstitial Zero-Point Energy (eV)	0.24	0.14	0.27	0.15
Corrected Binding Energy (eV)	0.35	0.39	0.77	0.96

The results reported in Table 1 show that hydrogen binding is endothermic versus the chosen free molecular H_2 reference state employed here for all the situations encountered. These values are consistent with experimentally measured H solution enthalpies [64, 65]of 0.25 eV, and 0.6 eV in Fe and Cr respectively. In that study the authors utilized the more stable antiferromagnetic arrangement of Cr but this did not significantly affect the binding energy as reported in Table 1. From Table 1, it may be concluded that the T-sites are more stable for binding H than the O-sites in both Fe and Cr and this observation is again in accordance with previous works [27, 64, 66]. Furthermore, the observed difference in H-binding energy between the T-sites and O-sites of about 0.15 eV for Fe is in accordance with Jiang and Carter, who report a difference of 0.13 eV [27].The zero-point energies reported for the interstitial sites in Fe also agree with the results of Hayward and Fu[66].

In determining the energies reported in Table 1, we required the energy of the hydrogen atom (half the energy of the hydrogen molecule) and the zero-point contribution to its energy. These values were obtained from placing a hydrogen molecule in a 10Å×10Å ×10Å box and allowing it to relax. This yielded an H-H bond length of 0.75 Å, consistent with previous studies. The internal energy and zero-point energy contribution per H were found as 3.38 eV/H and 0.134 eV/H, again consistent with previous work [27, 66]. However, it should be noted that these values have no bearing on the kMC simulations described later as they define a constant energy reference that identically cancels out when comparing the energy of different sites in the bulk. The hop frequency was estimated by assuming harmonic potential wells via the Vineyard approach [59] to be 3×10^{13} Hz. This number was calculated by applying the Vineyard approach [59]to calculate the hop frequency for H in bcc iron and H in bcc chromium and then interpolating between averaging the two numbers (31.9 THz for Cr and 27.4 THz for iron). The hop frequency in pure Fe and pure Cr was calculated by displacing the hydrogen atom only for calculation of the dynamical matrix by a finite difference approach, which has been shown to be accurate to within 25% [67]. Furthermore, the hop frequency was only calculated for the short T-site to T-site hop and it was not explicitly calculated for the pathway involving the octahedral site. The same hop frequency was used for hopping in all directions for all pathways.

Fitting the cluster expansion model

Next, the localized cluster expansion described in equation 1 was utilized to fit the DFT database generated of uncorrected binding energies of H in various Fe-Cr alloys. The fitting procedure weighted the pure iron and pure chromium binding energies more heavily (by a factor of 10) than the other structures in the database. (Not weighting the end points resulted in a CE that did not

predict H to be most stable in pure Fe.) The fit included 15 parameters in total and the results of the fit are summarized below.

Table 2. The derived effective cluster interactions along with the distances, d, in each figure. In the table, nn. refers to nearest neighbor.

Parameter	Value (eV)
Zero Body J_0	0.52
One Body J_{11} (1st nn.) ($d = a\frac{\sqrt{5}}{4}$)	0.026
One Body J_{12} (2nd nn.) ($d = a\frac{\sqrt{13}}{4}$)	0.058
One Body J_{13} (3rd nn.) ($d = a\frac{\sqrt{21}}{4}$)	0.007
One Body J_{14} (4th nn.) ($d = a\frac{\sqrt{29}}{4}$)	0.030
Two Body J_{21} ($d_1 = d_2 = a\frac{\sqrt{5}}{4}, d_3 = a\frac{\sqrt{3}}{2}$)	0.044
Two Body J_{22} ($d_1 = d_2 = a\frac{\sqrt{5}}{4}, d_3 = a$)	-0.002
Two Body J_{23} ($d_1 = a\frac{\sqrt{5}}{4}, d_2 = a\frac{\sqrt{13}}{4}, d_3 = a\frac{\sqrt{3}}{2}$)	-0.095
Two Body J_{24} ($d_1 = a\frac{\sqrt{5}}{4}, d_2 = a\frac{\sqrt{13}}{4}, d_3 = a$)	-0.013
Two Body J_{25} ($d_1 = a\frac{\sqrt{5}}{4}, d_2 = a\frac{\sqrt{13}}{4}, d_3 = a\sqrt{2}$)	-0.043
Two Body J_{26} ($d_1 = a\frac{\sqrt{13}}{4}, d_2 = a\frac{\sqrt{13}}{4}, d_3 = a$)	0.036
Three Body J_{31} (connects T-site to 3 1st nn.'s)	0.087
Three Body J_{32} (connects T-site to 2 1st nn.'s and 1 2nd nn., largest dist = $a\sqrt{2}$)	0.009
Three Body J_{43} (2 1st nn. and 1 2nd nn, largest dist = $a\frac{\sqrt{3}}{2}$)	0.004

Four Body (connects T-site to 4 1st nn.'s)	-0.009

The resulting CE is reasonably good at predicting DFT-derived binding energies as evidenced by the parity plot in Figure 1a, which shows the data points clustered about the y=x line. The root mean square error (RMSE) of the fit was 0.032 eV with a leave-one-out cross validation (LOOCV) score of 0.028 eV. In addition, the fit was found to be stable by checking that the histogram of the parameters recorded during the LOOCV procedure followed a normal distribution similar to previous work [68]. Finally, the variation of the binding energy as a function of the local environment is displayed in Figure 1b. It is evident that the binding energy increases with increasing local Cr content. Furthermore, the cluster expansion predicts the variation in the qualitative behavior of the binding energy as a function of the local environment. Here a caveat should be mentioned vis a vis alloys in the intermediate composition regime which were not directly included in the DFT database (although some of the intermediate compositions were captured in the local chemical environment of the hydrogen in a given cell). This is because we were more interested in capturing the physically relevant phenomena which occur in the low and high Cr concentration regimes. Limited testing of the model revealed that it may reasonably predict the binding energies in this regime. However, systematic benchmarking in this regime was not performed and therefore, the results of our model with regards to this regime must be viewed with caution.

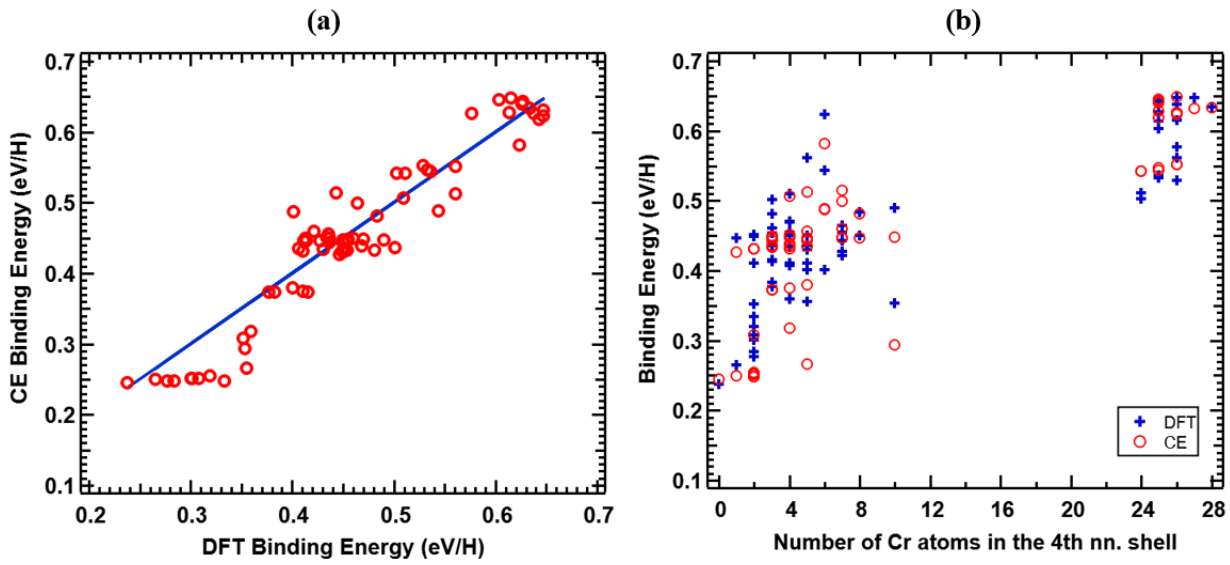

Figure 1. The cluster expansion fit to the DFT binding energy data. (a) A parity plot showing the agreement between the DFT recorded data and the cluster expansion (CE) model. The data points are clustered about the y=x line (b) The variation of the uncorrected binding energy as a function of the local environment up to the third nearest neighbor shell inclusive. Both the calculated DFT results (red circles) and the cluster expansion results (blue + signs) are shown.

In the kMC model, the contribution of the zero-point energy to the overall binding energy was taken into account by interpolating between the T-site zero-point energies for Fe and Cr based on the environment of the four 1st nearest neighboring bcc atoms. This methodology was tested for two different H atoms at T-sites in the $Fe_{0.8}Cr_{0.2}$ and $Fe_{0.1}Cr_{0.9}$ alloys and it was observed that this simple interpolation methodology led to fair agreement with the DFT calculation to within 0.013 eV.

The energetics in Figure 1b clearly show that the binding energy of H is strongly influenced by the metal environment. This is highlighted in Figure 2 where we examine the effect of including one Cr atom in a 2×2×2 bcc supercell (containing 1Cr atom and 15 Fe atoms) on the energy of H at the various T sites in the cell. Figures 2a-b show that the inclusion of 1 Cr atom (at 6.25 atomic %) leads to a significant perturbation of the binding energy landscape as predicted by the

cluster expansion. Moreover, Figure 2a clearly illustrates the long-range effects of this perturbation, which appears to affect a significant portion of the supercell. That is, the addition of Cr not only impacts the energetics of H in the nearest neighbor sites, but also those further away. This has implications for how H migrates in the alloy.

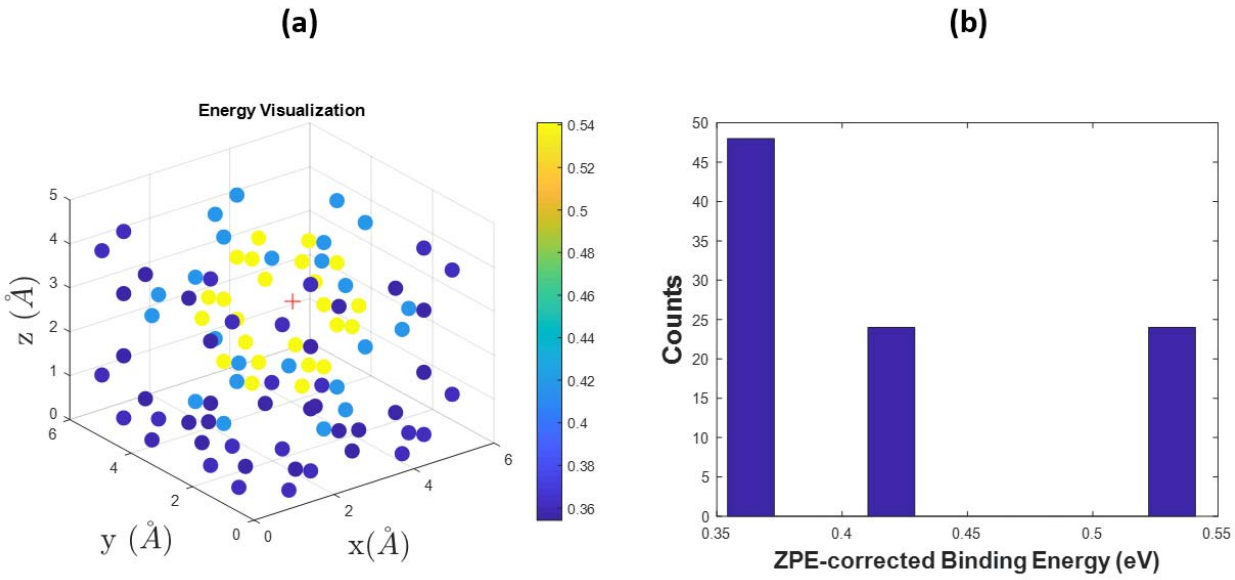

Figure 2. (a) A map of the CE-model predicted zero-point energy-corrected binding energy landscape of the system for a 2×2×2 supercell containing one Cr atom (0.0625 at%). The location of the Cr atom is shown with a red (+) sign and periodic boundary conditions are utilized. (b) A histogram of the energy landscape for the given situation showing the number of T binding sites within the cell calculated to have an H binding energy within a given range.

As a further illustration of the effects of including Cr atoms in bcc Fe supercells on the binding energy landscape, we plotted a series of energy landscape histograms as a function of the Cr content. The results are illustrated in Figure 3. In this case, we opted for large (50x50x50) supercells for better statistics. Clearly, as the concentration of Cr is initially increased, the landscape for H becomes much more heterogeneous. As the Cr concentration reaches very high levels, the H landscape becomes more homogeneous again.

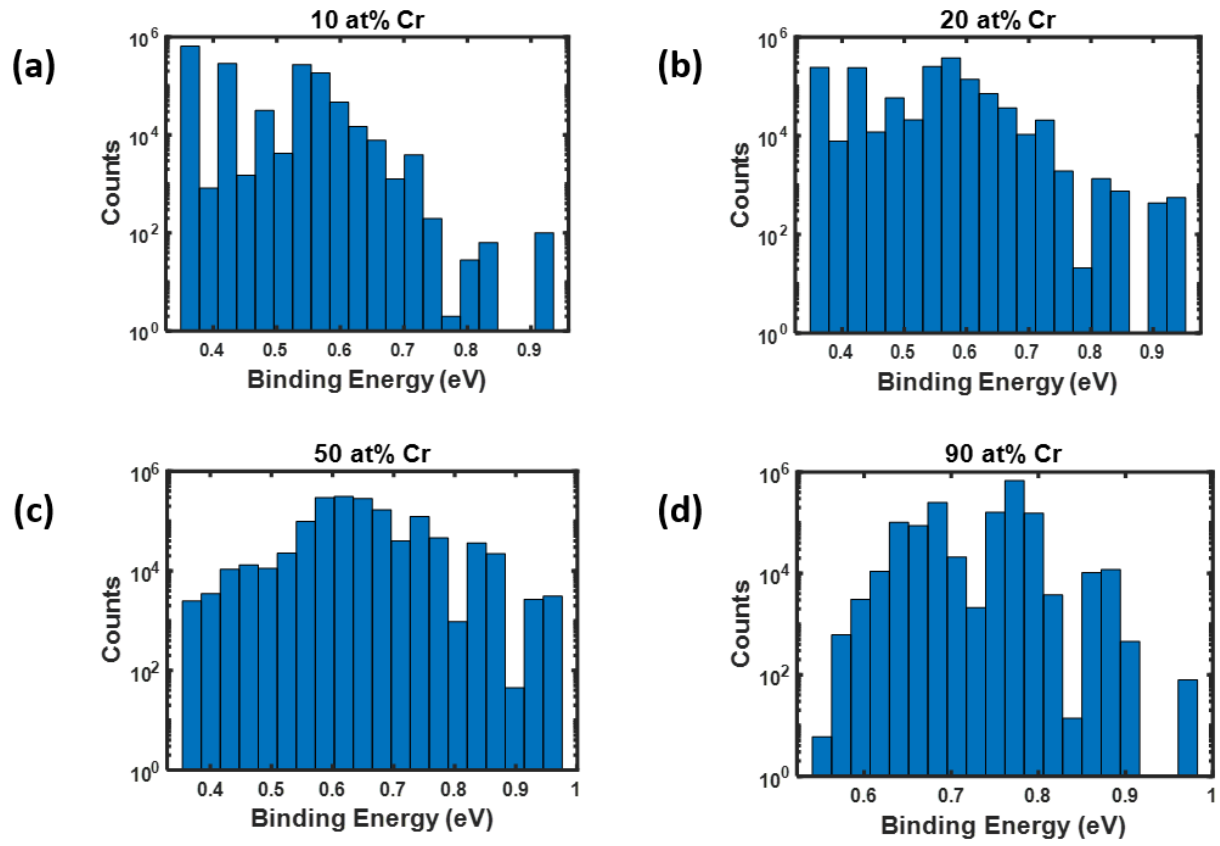

Figure 3. Semi-log plots of histograms of the binding energy landscape for a 50×50×50 bcc supercell with differing Cr content. The Cr atoms were randomly distributed in each case (a) 10 atomic% Cr (b) 20 atomic % Cr (c) 50 atomic% Cr (d) 90 atomic % Cr.

It should be mentioned however that in all cases represented in Figures 3a-3d, we observe T-sites with ZPE-corrected energy levels larger than that predicted for pure Cr (0.77 eV). This is believed to be an artifact of our cluster expansion model.

B. A model for the saddle energies

With the site energies reasonably well described by the CE, the final ingredient to perform the kMC simulations of transport is the saddle point energetics. The saddle point energies for the T-T and T-O-T pathways both in pure Fe and pure Cr were determined using CI-NEB. The energy barriers for the T-T and T-O-T pathways in Fe were determined to be 0.0449 eV and 0.0447 eV respectively. Similarly, in Cr the T-T and T-O-T pathway barriers were found to be 0.0623 eV

and 0.047 eV respectively. All the energy barrier values reported here include zero-point energy corrections for the ground T/O and activated transition states. The values reported for Fe are in good agreement with ZPE-corrected barriers reported in the literature. Jiang and Carter reported a barrier of 0.042 eV [27] while Hayward et al. reported a T-T barrier of 0.044 eV and a T-O-T pathway barrier of 0.035 eV for bcc Fe [66]. In order to address the barriers in the alloy, we utilized the model described by equation 2. The model includes two contributions: one that describes the energy difference between the final and initial state and another that describes a base barrier (E_o). This base barrier was actually computed by interpolating the base barriers for the pure Fe and pure Cr cases based on the nearest neighbor compositions of the initial and final states. This model was utilized in order to reduce the computational effort it would entail to build a DFT-derived database of saddle point energies. G

In order to test the validity of the proposed model, we tested four different cases where T-T and T-O-T pathway barriers were computed directly from DFT for different Cr environments. Our model led to errors less than 0.02 eV in the barriers for all cases when compared with the DFT . Therefore, while we recognize that this model is not exact, we believe it should be able to capture the dominant features of hydrogen diffusion in the Fe-Cr alloys.

D. Results from kMC simulations: homogeneous alloys

The model of equation (2) was utilized along with the cluster expansion to examine H diffusion in the Fe-Cr alloy as a function of composition and temperature. We examined two scenarios, one in which the Cr is randomly and homogeneously distributed and another in which the distribution is heterogeneous, mimicking the situation that might occur during radiation-induced segregation (RIS) [42, 52, 53]. The results for the homogeneous distributions are shown in Figure 4. For each concentration/temperature combination, we constructed three different

random representations of the alloy and then performed kMC simulations. All simulations were performed using 20×20×20 supercells of the alloy with 40 H atoms diffusing (0.25 atomic%) by averaging the mean square displacements of the 40 atoms per equation 4. Our cluster expansion model was mainly built from DFT databases in the low and high range of Cr content. However, the model has the ability to interpolate to intermediate compositions and we use it to examine the behavior of H diffusion in the full composition range. While the intermediate regime is not physical, as Fe and Cr are immiscible in this composition range, this still provides a useful reference for how H diffuses in alloys more generally.

From examining Figure 4 we observe that the diffusivity at all concentrations increases with temperature as expected. It is further observed that the diffusivity of H generally decreases with the addition of Cr and appears to be lowest around 50-70 atomic% of Cr content for all temperatures. This behavior may be explained on the basis of Figure 1. Hydrogen binding is more favorable in the Fe rich regions than it is in Cr rich regions. Thus, at high Cr concentrations, the hydrogen may be trapped in islands of Fe until it can overcome the energy barrier required to escape from these islands. It would then diffuse relatively quickly in the Cr rich regions until becoming trapped again in an Fe island. As the Cr concentration reaches a critical limit, it then begins to significantly influence the energy landscape of the now smaller iron islands and raise their energy (as illustrated in Figures 2a-b). This in turn makes it more likely for the hydrogen to overcome the energy barriers (the traps represented by the Fe islands are not as deep) and as a result we see that the diffusivity begins to increase again until it reaches its value in pure Cr. This conclusion may justify one key assumption made in a recent DFT work examining H diffusion in FeCr alloys where the authors considered the Cr-sites in the alloy to constitute “exclusion zones” [25]. Our results qualitatively agree with the study of Bruzzoni et

al.[25] who reported a drop of about 10% in the hydrogen diffusivity when Cr was introduced at a concentration of 6.25% (here we observed roughly a 10% drop in the diffusivity of H at 5% Cr at 300K compared with pure iron). In that study, the authors did not consider the T-O-T pathway and performed the simulation on a small supercell (16 atoms) which may have led to some finite size effects. Further, the authors' structures represent an ordered and periodic array of Cr in Fe. Nevertheless, it is encouraging to observe similar trends with the present model. In that study, the authors could only probe very dilute, fixed Cr concentrations. The advantage of our methodology is that it allows us to explore a wide range of phenomena over a large range of Cr concentrations. Finally, we expect that the general behavior represented in Figure 4 would be generic to many binary alloys depending on which metal the H more strongly binds to.

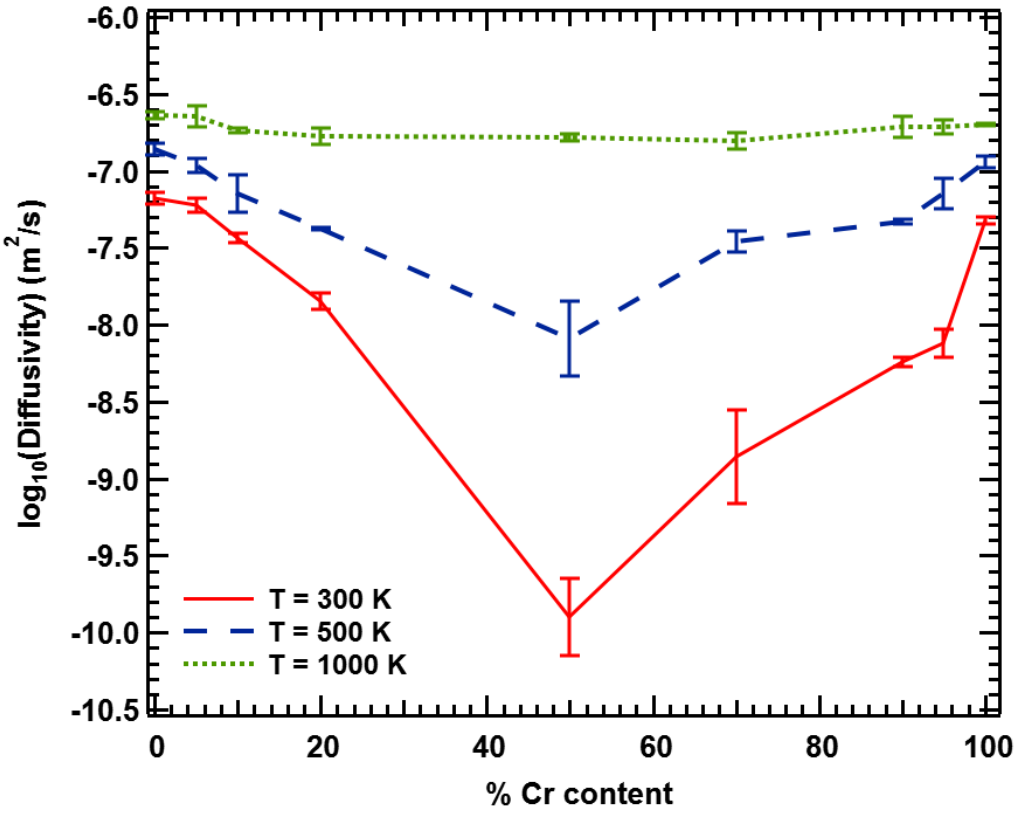

Figure 4. Diffusivity as a function of temperature and the chromium content in the random Fe-Cr alloy. The markers indicate the data points obtained in this study and the lines are used to help guide the eyes. Error bars

representing the uncertainty were also included from analyzing repeated simulations with different configurations..

The diffusivity results from Figure 4 were analyzed by plotting (1/T) vs. (ln(D)) for all three temperatures at each composition and then fitting a line in order to derive a general Arrhenius expression of the form $D = D_o e^{-\frac{E_a}{k_B T}}$ where E_a denotes the effective activation energy. The results are contained in Table 3.

Table 3. The results of Arrhenius fits of the recovered diffusivity data at three temperatures (T = 300K, 500K, 1000K)

% Cr content	**0%**	**10%**	**20%**	**50%**	**70%**	**90%**	**100%**
Activation Energy (eV)	0.046	0.058	0.09	0.26	0.19	0.13	0.056
D_o (m^2/s)	4×10^{-7}	3.3×10^{-7}	4.3×10^{-7}	36.3×10^{-7}	18.4×10^{-7}	9×10^{-7}	3.7×10^{-7}

From examining Table 3, we find that the activation energy for Fe (0%) is about the same as the reported barriers for T-T and T-O-T pathways (0.0446eV and 0.0449 eV), as should be expected. The same is true for the case of Cr (100%), where E^a is between the values for the two barriers (0.046 eV and 0.062 eV). We further notice that the activation energy increases monotonically from 0% to 50% Cr content before it decreases monotonically with increasing Cr content. This is due to the isolated Fe islands where the trapping of hydrogen may occur. This result is consistent with the experimental observations of Penalva et al.[69] who studied hydrogen transport in pure Fe, Fe5%Cr and Fe10%Cr for temperatures ranging from 423 K to 823 K and observed an increase in the activation energies derived from Arrhenius fits with increasing the Cr content.

E. Results from kMC simulations: heterogeneous Cr distributions

Finally, we investigated the effects of inhomogeneities in the material composition. This scenario may be of interest for applications involving radiation damage where areas of high Cr concentration (α′ precipitates) are known to form as well as other applications for composites. Further, RIS can lead to Cr-enriched interfaces (at least at temperatures below 700 C)[39-41] that, to first order, may be viewed as Cr rich slabs embedded in an Fe matrix. Finally, this scenario is representative of any alloy in which there is significant segregation of a solute to internal interfaces. The investigation was accomplished by utilizing 20×20×20 simulation cells with layers of alternating composition along the z-direction, as illustrated in Figure 5. The simulations were performed at a high temperature (T = 1000K) in order to obtain reasonable statistics for calculating the diffusivity in the z-direction.

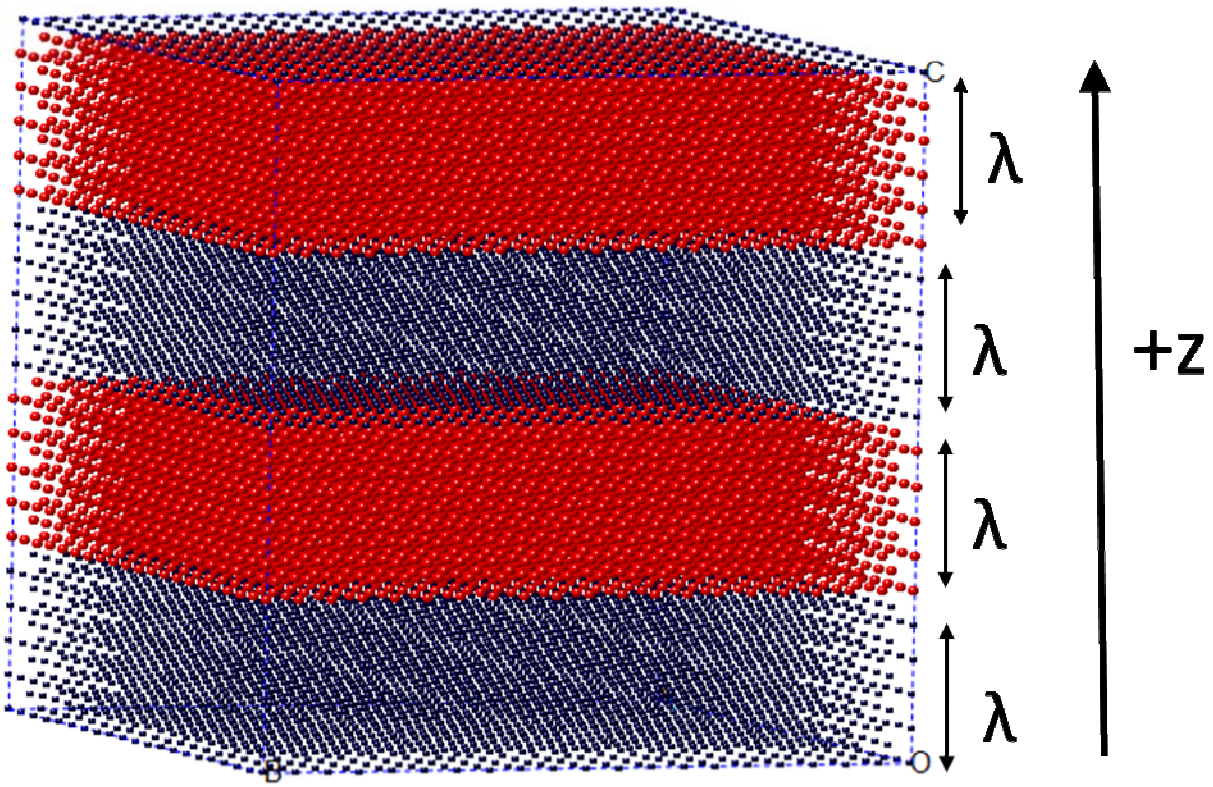

Figure 5. Illustration of the cell used for exploring the effects of inhomogeneities. In our investigation, we selected blocks of size λ along the z-direction. λ was expressed as integers of the unit cell and we examined the following cases: λ=1a, 2a, 5a, and 10a. For each of these cases we investigated two situations: one in which the alternating layers had compositions of 0% Cr and 100% Cr for an overall composition of 50 atomic% Cr; and another in which the alternating layers had compositions of 0% Cr and 40% Cr for a total composition of 20 atomic %Cr.

Two cases were considered in this work. In each case, the thickness of the layer along the z-direction (denoted by λ and measured in units of the lattice constant *a*) was varied and the diffusivities parallel and perpendicular to the z-direction were recorded. In case (a), the alternating layers had compositions of 100% Cr and 0% Cr for an overall average concentration of 50% Cr. In case (b), the alternating layers had the compositions of 40% Cr and 0% Cr for an average concentration of 20% Cr. Scenario (a) is representative of a condition in which

Radiation-Induced Segregation (RIS) occurs at interfaces and thus forms a potentially alpha-prime phase at those boundaries. In reality [4-6], the alpha-prime phase may not cover the entire interface but would form 3D precipitates. Further, segregation can occur to different extents in the real material. Thus, scenario (b) represents an intermediate scenario in which not enough Cr has segregated to precipitate alpha prime.

The simulations were carried out by again tracking 40 H atoms (with the site blocking model) and averaging their trajectories over 4×10^7 steps. The measured diffusivities are shown in Figure 6.

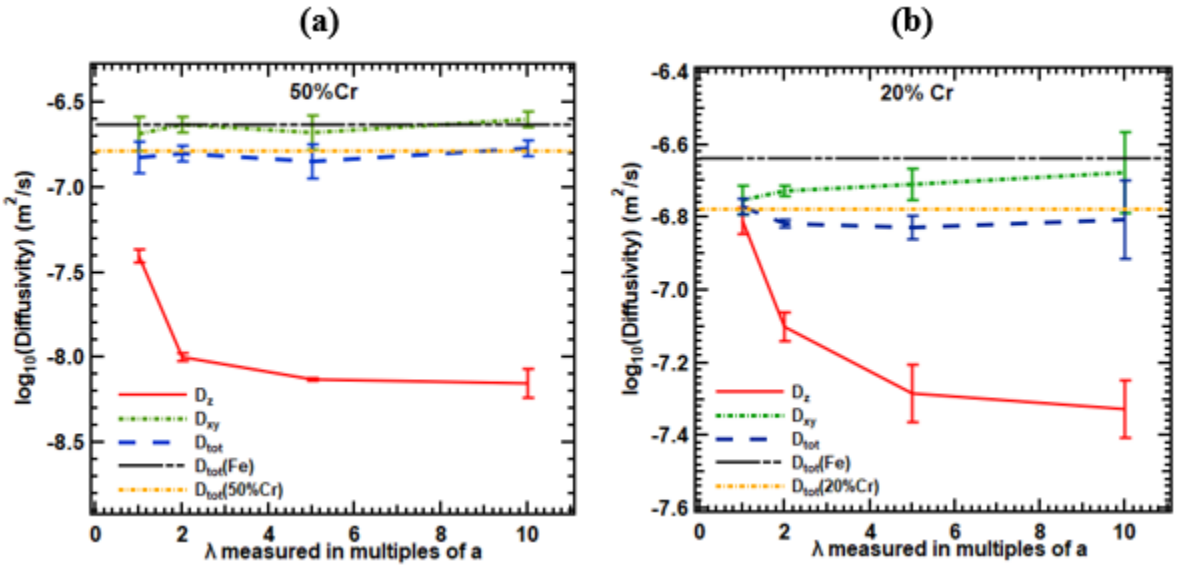

Figure 6. The effects of heterogeneous alloy composition on calculated diffusivity. In each simulation the simulation box was composed of (a) alternating layers in the z-direction containing 100% Cr and 0% Cr for an average of 50% Cr composition and (b) alternating layers of 40%Cr and 0%Cr for an average composition of 20% Cr. In each simulation, the thickness of the layer was denoted by λ (in units of the lattice constant). All simulations were performed in a 20×20×20 box. The diffusivity perpendicular to the direction of alternating layers (D_z) is shown with red solid lines, the diffusivity parallel to the direction of the layering (D_{xy}) is shown with green dotted lines, and the total diffusivity is shown with blue broken lines. The dashed black lines represent the diffusivity in pure iron and has been included for reference. The dotted yellow lines represent the diffusivity in the random alloy corresponding to the overall composition of the given simulation and has also been included for reference. The error bars have been included for the collected data points and the lines between the data points were added to guide the eye.

Upon inspection of Figure 6a and 6b, it appears the total diffusivity in both cases is similar to the expected value in the random alloy. Moreover, the changes in the total diffusivity and the diffusivity in the xy plane are small compared with the changes in the z-direction, regardless of composition. The diffusivity in the direction perpendicular to the layers (D_z) decreases with increasing layer thickness (λ) in both cases. As might be expected, the drop in diffusivity along z is greater for case (a), in which the Cr layers are pure Cr, as pure Cr acts as a larger barrier to H transport. More interestingly, we see that D_z is very sensitive to λ, especially for small λ. Further, the λ dependence is more gradual for case (b) than for case (a). Both of these effects are examined in more detail in what follows.

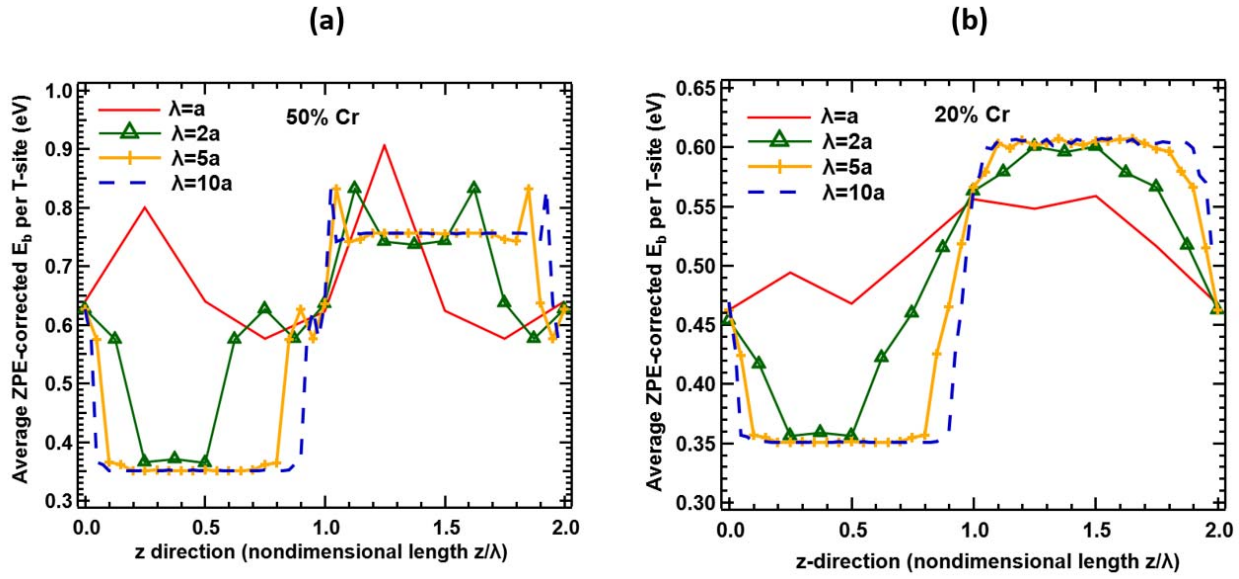

Figure 7. The ZPE-corrected hydrogen binding energy landscape of the structures being investigated by introducing inhomogeneities averaged for all T-site positions in the same xy-plane. The figure outlines the variation in the average binding energy landscape along the z-direction.

In order to gain better insight into the increase in D_z for small λ, we plotted the averaged ZPE-corrected binding energies as a function of z for all cases under scrutiny and the results are shown in Figure 7. From examining Figures 7 a and b, we find that for case (a) the binding energy landscape exhibits relatively large variations ranging from 0.35 to 0.85 eV compared with

the variations observed for case (b) ranging from 0.35 to 0.60 eV for the most extreme scenarios. As noted above, this is the reason that D_z is overall lower for case (a) than for case (b). Further, for both cases (a) and (b) we find that, for λ=1a, the energy wells are relatively shallow compared with the other cases and therefore the energy barriers are not as large. Hence, a drop in the diffusivity in the z-direction going from λ=a to λ=2a is expected and indeed observed in both cases. This is in fact the most pronounced effect observed for both cases and it is the case where the largest drop in D_z is observed. In addition, the observations are congruent with our understanding of the energy landscape from Figure 2 where it was shown that substituting one Cr atom for an Fe atom in a 16-atom supercell significantly affected the landscape and raised the energy levels of the T-sites within several nearest neighbor shells about the Cr atom. Therefore, by increasing the Fe layer thickness beyond a critical point where the Cr atoms do not raise the energy levels of all the T-sites within the Fe layer, an environment of pure iron is encountered by the H atoms with a deeper energy well to escape from compared with the λ=1a case.

Second, case (b), in which the Cr layers are not pure Cr, shows a more gradual dependence on λ than case (a). That is, in case (a), the pure Cr layers acts as a more consistent barrier to hydrogen transport, regardless of thickness, than case (b). This is a consequence of the detailed energy landscape within the Cr layers, as illustrated in Figure 8. For the case with pure Cr layers (Figure 8a), the hydrogen energy landscape is uniform and this would be true regardless of layer thickness. However, for case (b), in which the Cr layers only contain 40% Cr content, the distributions are random within the Cr layers and there are potential low energy pathways that span the Cr layer, allowing hydrogen to migrate through the Cr layer. Further, the probability of such pathways is decreased as λ is increased, as can be seen by comparing Figure 8b and 8c.

Thus, in the case of a Cr layer with a random distribution of Fe, the ability of hydrogen to easily diffuse through the layer depends on the layer thickness.

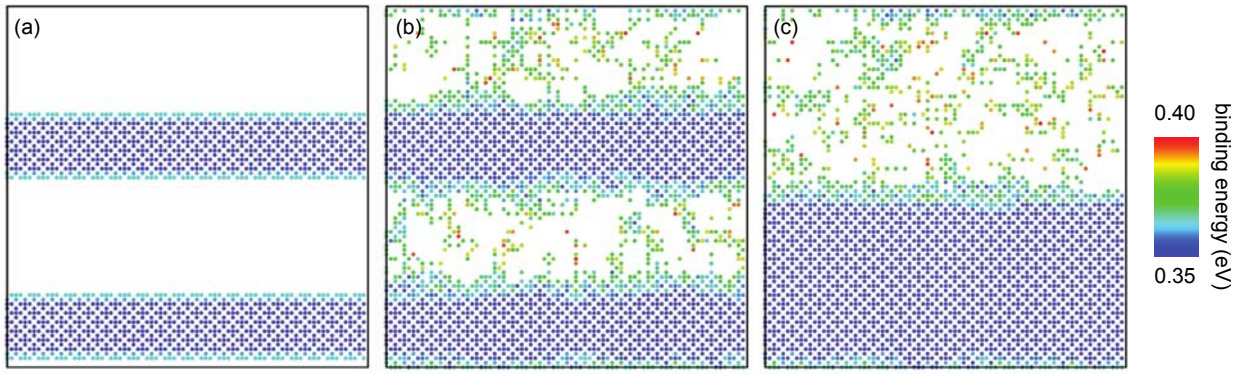

Figure 8. Map of the energy of tetrahedral sites within multilayer configurations with (a) layers of 0% and 100% Cr and λ=5a, (b) layers of 0% and 40% Cr and λ=5a, and (c) layers of 0% and 40% Cr and λ=5a. Only sites with energies within 0.05 eV of the lowest energy site (about 0.35 eV) are shown. The dark blue layers are indicative of the pure Fe layers.

It is useful to consider the behavior of the diffusivity in the infinite λ limit. If $\lambda \rightarrow \infty$ but time is finite, hydrogen would most likely only be able to sample the Fe region of the material. Thus, we would expect that, on experimental time scales, unless the experiment was directly measuring across the Cr profile, the diffusivity of hydrogen would approach that in pure Fe. In this case, as λ increases, we would expect D_z to eventually rise and converge with D_x and D_y. However, if one could sample over an infinite time, then the Cr layers would reassert themselves on the diffusivity and the diffusivity would approach that of multilayer system. In this case, D_z would always be less than D_x and D_y. Thus, the nature of the experiment would dictate what behavior is sampled and the consequence on the measured diffusivity.

Given that the hopping barriers for hydrogen in iron and chromium are relatively small and very similar, the binding energies of hydrogen in the different metals play the dominant role in

dictating and predicting transport in alloys. To observe the effects of segregation more clearly, we considered a different scenario. Here we examined two supercells that mimic a three-dimensional grain with solute segregation to the "grain boundaries," or edges of the cell. In the first, the interior of the supercell was composed entirely of iron and the boundaries of chromium. In the second case, we considered the interior of the cell to be composed entirely of Cr and the boundaries of Fe. The simulation cell concept is illustrated in Figure 9. These scenarios were introduced in an attempt to mimic real-life situations which lead to segregation such as radiation damage, which causes the chromium to segregate to or away from the boundaries.

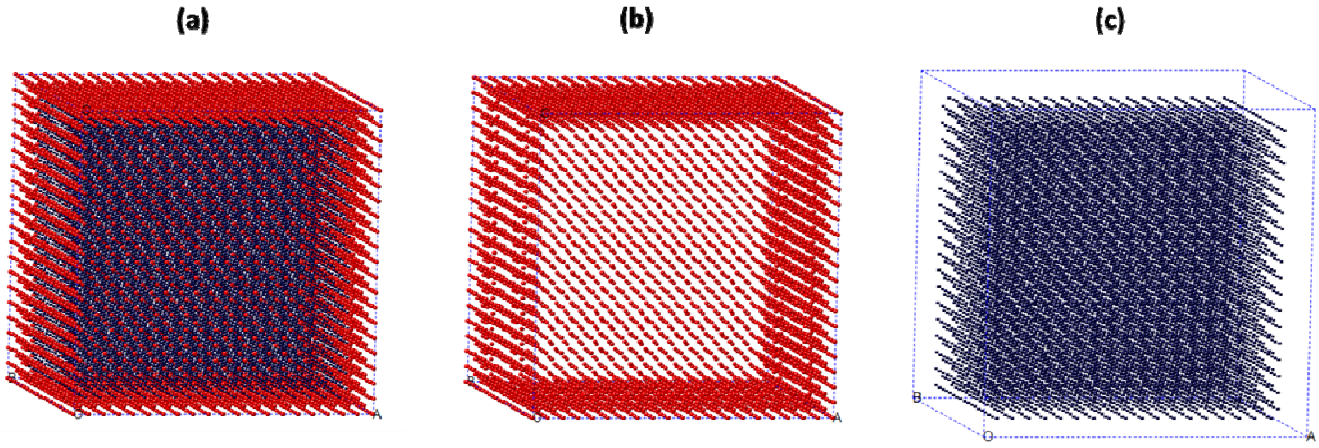

Figure 9. An illustration of the supercell considered for studying inhomogeneities which mimics the situation of a grain and a grain boundary. Structure (a) shows the entire supercell. Structure (b) illustrates the element that occupies the grain boundary and structure (c) illustrates the element occupying the grain (the inside of the supercell). We considered two cases in our study: Case 1: The grain is composed of Fe and the grain boundary of Cr. Case 2: The grain is composed of Cr and the grain boundary of Fe.

As opposed to the geometries in Figure 5, in these situations, transport in all three directions is confined by a zone of another element that the hydrogen atoms must overcome. The hydrogen is more stable in iron (a smaller binding energy) and, therefore, when iron occupies the boundaries of the cell, it is expected that the hydrogen stays in the iron and has a high diffusivity compared with the case where chromium occupies the boundaries of the cell. Essentially, when iron occupies the boundaries of the cell (the grain boundary), the connected iron grain boundaries

(GBs) provide a fast pathway for diffusion for the hydrogen, whereas for the case where the chromium occupies the boundaries of the cell, the hydrogen becomes trapped in the iron inside the cell and the diffusivity is expected to be smaller. Indeed, by performing two simulations for the cases of Fe in the grain vs. Fe in the grain boundary (using 40 hydrogen atoms, at 500 K, in 20x20x20 supercells where 27% of the atoms were boundary atoms) we calculated diffusivities (per H atom) of 3.5×10^{-10} m^2/s and 9.5×10^{-8} m^2/s, respectively, a factor of nearly 300.

Discussion:

A key observation of our simulations is that, as solutes segregate within a matrix, they can either impede or enhance hydrogen transport. In the case of Fe-Cr alloys, this is driven by the relative binding energy of hydrogen in Fe versus Cr. Based on this observation, we can extrapolate the results to other alloys using the binding energies for hydrogen as a qualitative indicator of hydrogen transport. For example, Pd is expected to segregate to grain boundaries in matrices of Cr and Cu [70] while Cr may segregate to the boundaries of a Pd matrix. Furthermore, based on ab initio calculated binding energies [63, 64] which show hydrogen to be more stable in Pd than in Cu or Cr then it may be expected that the diffusivity of hydrogen for cases where Pd is in the grain and Cr is in the grain boundary is slow compared with the case where Pd segregates to the grain boundary of a Cr matrix. Through similar arguments one can construct a chart of solutes versus solvents in which hydrogen transport may be enhanced or retarded compared to a homogeneous solid solution, as shown in Figure 10. The construction of this chart is based on that in Ref. [70], modulo the hydrogen binding energy of Refs. [63, 64]. That is, we consider hydrogen transport to be enhanced for cases in which hydrogen prefers to bind (by more than 0.1 eV) to the element that is in the grain boundaries (the solute for cases of segregation, the solvent for cases of desegregation, as indicated in Ref. [70]). The degree of enhancement or retardation,

as indicated in Figure 10, is a reflection of the strength of segregation or desegregation as reported in Ref. [70]. This analysis assumes that, as we have seen for Fe-Cr, the diffusivity is dominated by binding energies and not differences in base mobility in each metal. Even so, it provides an initial basis for screening for alloy systems in which hydrogen transport can be modified by solute segregation.

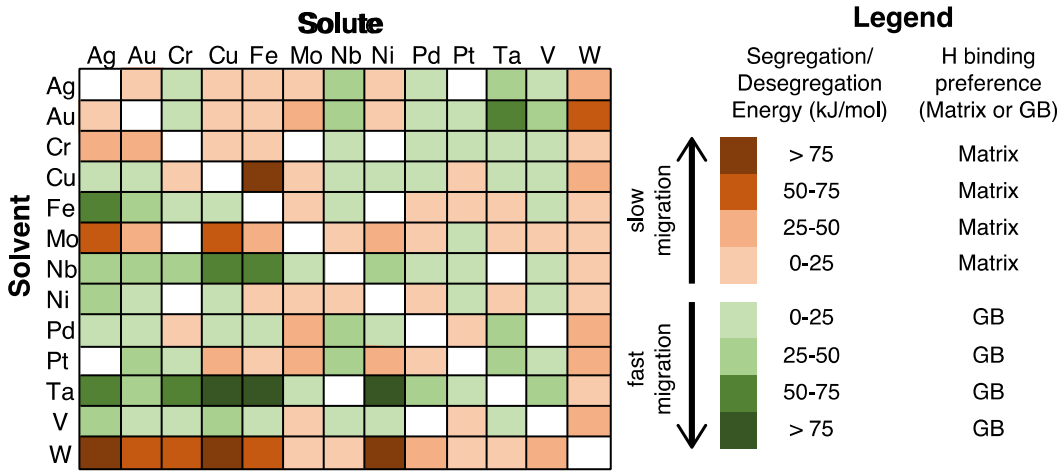

Figure 10.Chart highlighting solute/solvent combinations that are expected to enhance (green) or retard (red) hydrogen transport as compared to a solid solution alloy. The shade of the color indicates the expected modification of transport as based on solute segregation energies report in Ref. [70]. Those segregation energies are modulated by predicted binding energies (from Refs. [63, 64]) to the different component metals. If H prefers to go to the metal that is enriched at the GB, transport would be fast. Otherwise, it would be slow.

Another implication of our results connects to the evolution of chemistry due to radiation-induced segregation. As Fe-Cr alloys are irradiated, the Cr redistributes in the material and can either segregate or desegregate to boundaries, depending on temperature [39-41]. At the temperatures of operation (below 700 C), Cr will segregate to boundaries as the fluence increases. Thus, as the material is irradiated, what might have started out as a relatively homogeneous alloy will become more and more heterogeneous, with more and more Cr at the grain boundaries. As schematically illustrated in Figure 11, this suggests that, as the material

experiences a larger radiation dose, hydrogen transport into the material will be impeded, and fewer hydrogen-like species (H, D, and T) will leak out into the coolant. Thus, while tritium leakage might be a concern for the fresh alloy [39], as radiation progresses, the issue might be mitigated to some degree. This is independent of any effects of radiation-induced defects, such as hydrogen trapping by high concentrations of radiation-induced vacancies.

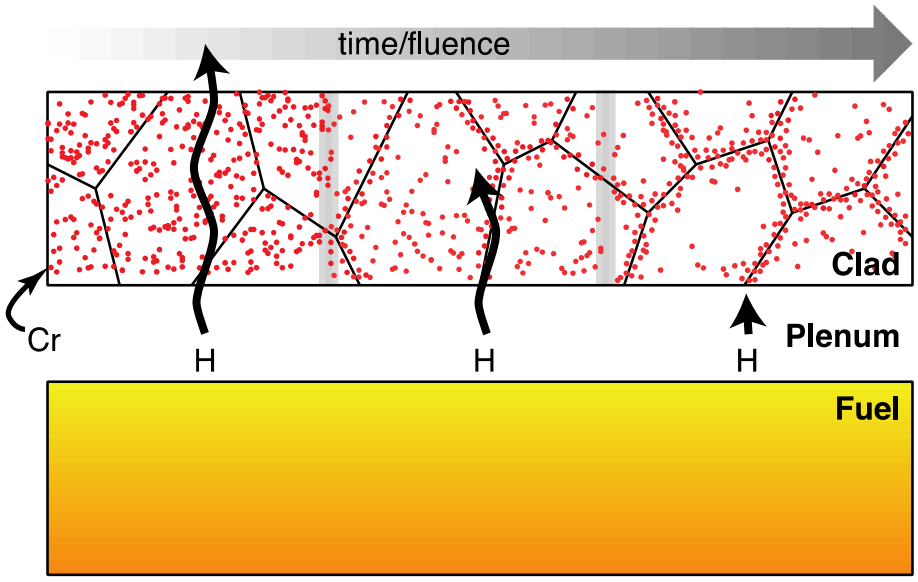

Figure 11. Schematic of how hydrogen transport through an Fe-Cr based alloy might be modified as the clad is irradiated. Burning the fuel produces hydrogen. Initially, when the Fe-Cr alloy is more chemically homogeneous (randomly distributed), hydrogen has the highest rate of transport through the alloy. As radiation progresses and radiation-induced segregation of Cr to grain boundaries increases, the transport of hydrogen through the clad will be reduced and the leakage through the clad into the coolant will be likewise reduced.

Finally, it is important to consider the limitations of the current study. In the present work we were primarily limited by the errors introduced by the cluster expansion representation of the energy and by the interpolation used to determine the zero-point energy corrections and the saddle point energies. However, while the detailed behavior of hydrogen in these alloys might not be entirely faithful to the underlying DFT data, we expect that basic trends are well reproduced by our model. In addition, the binary alloys in the study were prepared by randomly choosing the iron and chromium atoms thereby completely neglecting the role of short range

order which may be present in real binary alloys. Furthermore, vacancies and other point defects, which are known to play an important role in trapping and transport of hydrogen under certain conditions [71, 72], were not considered here. The effects of internal strain and actual microstructure were also ignored. In addition, the kinetically resolved activation barrier model, while useful, may fail in some cases. While this issue is beyond the scope of the manuscript, it presents another limitation on our work.

It has also been demonstrated that the migration energies of defects do depend on the magnetic disordering due to finite temperatures[73]. Considerations regarding the magnetic structure are beyond the scope of our work and this issue represents another limitation. However, we attempt to discuss the consequences of antiferromagnetic ordering. First of all, it is important to keep in mind that the effects arising from the antiferromagnetic ordering will be confined only to the Cr rich compositions and this issue is not relevant for other compositions at lower Cr content. Secondly, and assuming all Cr-rich structures have a similar lowering of binding energy, then the diffusivity in the Cr-rich homogeneous alloys would remain similar to what we reported, as the potential energy landscape would simply shift by a constant value. In heterogeneous structures, Cr would have a weaker trapping effect on H transport than in our model and our results would underestimate the diffusivity in the perpendicular directions in the layered structures examined in Fig. 6. Finally, while this effect would impact the absolute numbers we report, it would not significantly affect the general trends nor our conclusions. Finally, our representation of interfaces neglects the actual structure of grain boundaries, which can also impact transport [74-76]. Nevertheless, we do not expect these effects to detract from the general conclusions of this study.

Conclusions:

In this work, DFT calculations of hydrogen binding in Fe-Cr alloys were coarse-grained through the use of a localized cluster expansion description of the potential function. In addition, energy barriers for hydrogen hopping were estimated by examining the local environments of the initial and final states. This description was shown to yield a reasonable agreement with the DFT results and was subsequently utilized in a kinetic Monte Carlo simulation. The results explored the behavior of hydrogen in the Fe-Cr alloys as a function of the Cr content and local chemical variations. For homogeneous random alloys, the hydrogen diffusivity was shown to decrease and then increase with increasing Cr content with the lowest levels of diffusivity observed around 50% Cr for all temperatures. This may be explained by the trapping of hydrogen in Fe rich areas as the Cr content increases. The effects of nanoscale heterogeneity were investigated by using slabs of alternating compositions and by increasing the thickness of these slabs. It was observed that the diffusivity in the perpendicular direction (relative to the direction of the alternating layers) could be significantly affected and was shown to decrease with increasing layer thickness. This behavior was rationalized by examining the energy landscape of hydrogen in the different structures. The results of this study allow us to generalize how hydrogen might diffuse in various solute/solvent combinations, providing some guidance on alloy systems in which hydrogen transport might be enhanced or impeded. Finally, our results also provide some insight into how hydrogen transport might change in the evolving microstructure of an irradiated Fe-Cr clad.

Acknowledgements:

Research primarily supported by the LANL Laboratory Directed Research and Development (LDRD) program (AJS, conceptual design of study, development of model and execution of simulations). In addition, EFH and BPU acknowledge support as part of FUTURE (Fundamental Understanding of Transport Under Reactor Extremes), an Energy Frontier Research Center funded by the U.S. Department of Energy (DOE), Office of Science, Basic Energy Sciences (BES) (conceptual design of study, interpretation of results). AJS primarily wrote the

manuscript, but all authors contributed to the writing and editing of the manuscript. Computational support through Los Alamos National Laboratory Institutional Computing is gratefully acknowledged. Los Alamos National Laboratory is operated by Los Alamos National Security, LLC, for the National Nuclear Security Administration of the (U.S.) Department of Energy under contract DE-AC52-06NA25396.

References:

1. Dadfarnia, M., et al., *Recent Advances in the Study of Structural Materials Compatibility with Hydrogen.* Advanced Materials, 2010. **22**(10): p. 1128-1135.
2. Song, J. and W.A. Curtin, *Atomic mechanism and prediction of hydrogen embrittlement in iron.* Nature Materials, 2012. **12**: p. 145.
3. Hardie, D., E.A. Charles, and A.H. Lopez, *Hydrogen embrittlement of high strength pipeline steels.* Corrosion Science, 2006. **48**(12): p. 4378-4385.
4. Rodrigues, D.C., et al., *In vivo severe corrosion and hydrogen embrittlement of retrieved modular body titanium alloy hip-implants.* Journal of Biomedical Materials Research Part B: Applied Biomaterials, 2009. **88B**(1): p. 206-219.
5. Asaoka, K., K. Yokoyama, and M. Nagumo, *Hydrogen embrittlement of nickel-titanium alloy in biological environment.* Metallurgical and Materials Transactions A, 2002. **33**(3): p. 495-501.
6. Dadfarnia, M., et al., *Recent advances on hydrogen embrittlement of structural materials.* International Journal of Fracture, 2015. **196**(1): p. 223-243.
7. Bechtle, S., et al., *Grain-boundary engineering markedly reduces susceptibility to intergranular hydrogen embrittlement in metallic materials.* Acta Materialia, 2009. **57**(14): p. 4148-4157.
8. Marchi, C.S., B.P. Somerday, and S.L. Robinson, *Permeability, solubility and diffusivity of hydrogen isotopes in stainless steels at high gas pressures.* International Journal of Hydrogen Energy, 2007. **32**(1): p. 100-116.
9. Sakintuna, B., F. Lamari-Darkrim, and M. Hirscher, *Metal hydride materials for solid hydrogen storage: A review.* International Journal of Hydrogen Energy, 2007. **32**(9): p. 1121-1140.
10. Hatano, Y., et al., *Deuterium trapping at defects created with neutron and ion irradiations in tungsten.* Nuclear Fusion, 2013. **53**(7): p. 073006.
11. Markelj, S., et al., *Deuterium retention in tungsten simultaneously damaged by high energy W ions and loaded by D atoms.* Nuclear Materials and Energy, 2017. **12**: p. 169-174.
12. Senkov, O.n. and F.H. Froes, *Thermohydrogen processing of titanium alloys.* International Journal of Hydrogen Energy, 1999. **24**(6): p. 565-576.
13. Yamamoto, Y., et al., *Development and property evaluation of nuclear grade wrought FeCrAl fuel cladding for light water reactors.* Journal of Nuclear Materials, 2015. **467**: p. 703-716.
14. Terrani, K.A., S.J. Zinkle, and L.L. Snead, *Advanced oxidation-resistant iron-based alloys for LWR fuel cladding.* Journal of Nuclear Materials, 2014. **448**(1): p. 420-435.
15. Cook, I., *Materials research for fusion energy.* Nature Materials, 2006. **5**: p. 77.
16. Baluc, N., et al., *On the potentiality of using ferritic/martensitic steels as structural materials for fusion reactors.* Nuclear Fusion, 2004. **44**(1): p. 56.
17. Sachitanand, R., et al., *Evaluation of the oxidation and Cr evaporation properties of selected FeCr alloys used as SOFC interconnects.* International Journal of Hydrogen Energy, 2013. **38**(35): p. 15328-15334.
18. Kurokawa, H., K. Kawamura, and T. Maruyama, *Oxidation behavior of Fe–16Cr alloy interconnect for SOFC under hydrogen potential gradient.* Solid State Ionics, 2004. **168**(1): p. 13-21.
19. Fazio, C., et al., *Innovative materials for Gen IV systems and transmutation facilities: The cross-cutting research project GETMAT.* Nuclear Engineering and Design, 2011. **241**(9): p. 3514-3520.

20. Kiejna, A. and E. Wachowicz, *Segregation of Cr impurities at bcc iron surfaces: First-principles calculations.* Physical Review B, 2008. **78**(11): p. 113403.
21. Shibuta, Y., S. Takamoto, and T. Suzuki, *Dependence of the grain boundary energy on the alloy composition in the bcc iron–chromium alloy: A molecular dynamics study.* Computational Materials Science, 2009. **44**(4): p. 1025-1029.
22. Dopico, I., P. Castrillo, and I. Martin-Bragado, *Quasi-atomistic modeling of the microstructure evolution in binary alloys and its application to the FeCr case.* Acta Materialia, 2015. **95**: p. 324-334.
23. Malerba, L., A. Caro, and J. Wallenius, *Multiscale modelling of radiation damage and phase transformations: The challenge of FeCr alloys.* Journal of Nuclear Materials, 2008. **382**(2): p. 112-125.
24. Kuronen, A., et al., *Segregation, precipitation, and α–α' phase separation in Fe-Cr alloys.* Physical Review B, 2015. **92**(21): p. 214113.
25. Bruzzoni, P. and R.C. Pasianot, *A DFT study of H solubility and diffusion in the Fe-Cr system.* Computational Materials Science, 2018. **154**: p. 243-250.
26. Hayward, E. and C.-C. Fu, *Interplay between hydrogen and vacancies in α-Fe.* Physical Review B, 2013. **87**(17): p. 174103.
27. Jiang, D.E. and E.A. Carter, *Diffusion of interstitial hydrogen into and through bcc Fe from first principles.* Physical Review B, 2004. **70**(6): p. 064102.
28. Bavrina, O.O., et al., *First-principle modeling of hydrogen site solubility and diffusion in disordered Ti–V–Cr alloys.* International Journal of Hydrogen Energy, 2018.
29. Tafen, D.N., *First-principles-based kinetic Monte Carlo studies of diffusion of hydrogen in Ni–Al and Ni–Fe binary alloys.* Journal of Materials Science, 2015. **50**(9): p. 3361-3370.
30. Volodin, A.A., et al., *Hydrogen diffusion in La1.5Nd0.5MgNi9 alloy electrodes of the Ni/MH battery.* Journal of Alloys and Compounds, 2015. **645**: p. S288-S291.
31. Alimov, V.N., et al., *Hydrogen transport through V–Pd alloy membranes: Hydrogen solution, permeation and diffusion.* Journal of Membrane Science, 2015. **481**: p. 54-62.
32. Sanchez, J., et al., *Hydrogen in α-iron: Stress and diffusion.* Physical Review B, 2008. **78**(1): p. 014113.
33. Du, Y.A., J. Rogal, and R. Drautz, *Diffusion of hydrogen within idealized grains of bcc Fe: A kinetic Monte Carlo study.* Physical Review B, 2012. **86**(17): p. 174110.
34. Peñalva, I., et al., *Influence of Cr content on the diffusive transport parameters and trapping of hydrogen in Fe alloys.* Fusion Engineering and Design, 2014. **89**(7): p. 1628-1632.
35. Ke, X. and G.J. Kramer, *Absorption and diffusion of hydrogen in palladium-silver alloys by density functional theory.* Physical Review B, 2002. **66**(18): p. 184304.
36. Kamakoti, P. and D.S. Sholl, *Ab initio lattice-gas modeling of interstitial hydrogen diffusion in CuPd alloys.* Physical Review B, 2005. **71**(1): p. 014301.
37. Semidey-Flecha, L. and D.S. Sholl, *Combining density functional theory and cluster expansion methods to predict H2 permeance through Pd-based binary alloy membranes.* The Journal of Chemical Physics, 2008. **128**(14): p. 144701.
38. Lu, Y., et al., *First-principles study of hydrogen behavior in vanadium-based binary alloy membranes for hydrogen separation.* International Journal of Hydrogen Energy, 2017. **42**(36): p. 22925-22932.
39. Terrani, K.A., *Accident tolerant fuel cladding development: Promise, status, and challenges.* Journal of Nuclear Materials, 2018. **501**: p. 13-30.
40. Wharry, J.P. and G.S. Was, *A systematic study of radiation-induced segregation in ferritic–martensitic alloys.* Journal of Nuclear Materials, 2013. **442**(1): p. 7-16.

41. Marquis, E.A., S. Lozano-Perez, and V.d. Castro, *Effects of heavy-ion irradiation on the grain boundary chemistry of an oxide-dispersion strengthened Fe–12wt.% Cr alloy.* Journal of Nuclear Materials, 2011. **417**(1): p. 257-261.
42. Martínez, E., et al., *Role of Sink Density in Nonequilibrium Chemical Redistribution in Alloys.* Physical Review Letters, 2018. **120**(10): p. 106101.
43. Wu, C.Z., et al., *Effect of carbon/noncarbon addition on hydrogen storage behaviors of magnesium hydride.* Journal of Alloys and Compounds, 2006. **414**(1): p. 259-264.
44. Jeon, K.-J., et al., *Air-stable magnesium nanocomposites provide rapid and high-capacity hydrogen storage without using heavy-metal catalysts.* Nature Materials, 2011. **10**: p. 286.
45. Farsak, M., et al., *The noble metal loading binary iron–zinc electrode for hydrogen production.* International Journal of Hydrogen Energy, 2017. **42**(10): p. 6455-6461.
46. Kresse, G. and J. Furthmüller, *Efficiency of ab-initio total energy calculations for metals and semiconductors using a plane-wave basis set.* Computational Materials Science, 1996. **6**(1): p. 15-50.
47. Blöchl, P.E., *Projector augmented-wave method.* Physical Review B, 1994. **50**(24): p. 17953-17979.
48. Kresse, G. and D. Joubert, *From ultrasoft pseudopotentials to the projector augmented-wave method.* Physical Review B, 1999. **59**(3): p. 1758-1775.
49. Perdew, J.P., K. Burke, and M. Ernzerhof, *Generalized Gradient Approximation Made Simple.* Physical Review Letters, 1996. **77**(18): p. 3865-3868.
50. Methfessel, M. and A.T. Paxton, *High-precision sampling for Brillouin-zone integration in metals.* Physical Review B, 1989. **40**(6): p. 3616-3621.
51. Monkhorst, H.J. and J.D. Pack, *Special points for Brillouin-zone integrations.* Physical Review B, 1976. **13**(12): p. 5188-5192.
52. Etienne, A., et al., *Comparison of radiation-induced segregation in ultrafine-grained and conventional 316 austenitic stainless steels.* Ultramicroscopy, 2011. **111**(6): p. 659-663.
53. Watanabe, S., et al., *Radiation-induced segregation at grain boundary in Fe-Cr-Ni alloy system: effect of temperature variation.* Journal of Nuclear Materials, 1996. **239**: p. 200-204.
54. Henkelman, G., B.P. Uberuaga, and H. Jónsson, *A climbing image nudged elastic band method for finding saddle points and minimum energy paths.* The Journal of Chemical Physics, 2000. **113**(22): p. 9901-9904.
55. Puchala, B. and D. Morgan, *Atomistic modeling of As diffusion in ZnO.* Physical Review B, 2012. **85**(6): p. 064106.
56. Van der Ven, A., et al., *First-principles theory of ionic diffusion with nondilute carriers.* Physical Review B, 2001. **64**(18): p. 184307.
57. Hlushkou, D., et al., *Numerical simulation of electrochemical desalination.* Journal of Physics: Condensed Matter, 2016. **28**(19): p. 194001.
58. Laidler, K.J. and M.C. King, *Development of transition-state theory.* The Journal of Physical Chemistry, 1983. **87**(15): p. 2657-2664.
59. Vineyard, G.H., *Frequency factors and isotope effects in solid state rate processes.* Journal of Physics and Chemistry of Solids, 1957. **3**(1): p. 121-127.
60. Birch, F., *Finite Elastic Strain of Cubic Crystals.* Physical Review, 1947. **71**(11): p. 809-824.
61. Murnaghan, F.D., *The Compressibility of Media under Extreme Pressures.* Proceedings of the National Academy of Sciences, 1944. **30**(9): p. 244-247.
62. Hafner, R., et al., *Magnetic ground state of Cr in density-functional theory.* Physical Review B, 2002. **65**(18): p. 184432.
63. You, Y.-W., et al., *Dissolving, trapping and detrapping mechanisms of hydrogen in bcc and fcc transition metals.* AIP Advances, 2013. **3**(1): p. 012118.

64. Ohsawa, K., et al., *Configuration and binding energy of multiple hydrogen atoms trapped in monovacancy in bcc transition metals.* Physical Review B, 2012. **85**(9): p. 094102.
65. Fukai, Y., *The metal-hydrogen system basic bulk properties*. 2nd ed. ed. 2005, Berlin

New York: Berlin : Springer.
66. Hayward, E. and C.-C. Fu, *Interplay between hydrogen and vacancies in $\ensuremath{\alpha}$-Fe.* Physical Review B, 2013. **87**(17): p. 174103.
67. Wu, H.H. and D.R. Trinkle, *Direct Diffusion through Interpenetrating Networks: Oxygen in Titanium.* Physical Review Letters, 2011. **107**(4): p. 045504.
68. Samin, A.J. and C.D. Taylor, *A first principles investigation of the oxygen adsorption on Zr(0001) surface using cluster expansions.* Applied Surface Science, 2017. **423**: p. 1035-1044.
69. Peñalva, I., et al., *Influence of the Cr content on the permeation of hydrogen in Fe alloys.* Journal of Nuclear Materials, 2013. **442**(1, Supplement 1): p. S719-S722.
70. Murdoch, H.A. and C.A. Schuh, *Estimation of grain boundary segregation enthalpy and its role in stable nanocrystalline alloy design.* Journal of Materials Research, 2013. **28**(16): p. 2154-2163.
71. Paxton, A.T. and I.H. Katzarov, *Quantum and isotope effects on hydrogen diffusion, trapping and escape in iron.* Acta Materialia, 2016. **103**: p. 71-76.
72. Johnson, D.F. and E.A. Carter, *Hydrogen in tungsten: Absorption, diffusion, vacancy trapping, and decohesion.* Journal of Materials Research, 2011. **25**(2): p. 315-327.
73. Sandberg, N., et al., *Modeling of the magnetic free energy of self-diffusion in bcc Fe.* Physical Review B, 2015. **92**(18): p. 184102.
74. Pedersen, A. and H. Jónsson, *Simulations of hydrogen diffusion at grain boundaries in aluminum.* Acta Materialia, 2009. **57**(14): p. 4036-4045.
75. Oudriss, A., et al., *Grain size and grain-boundary effects on diffusion and trapping of hydrogen in pure nickel.* Acta Materialia, 2012. **60**(19): p. 6814-6828.
76. Du, Y.A., et al., *First-principles study on the interaction of H interstitials with grain boundaries in $\ensuremath{\alpha}$- and $\ensuremath{\gamma}$-Fe.* Physical Review B, 2011. **84**(14): p. 144121.